

Optical Response of 3D Nano-Architecture Solar Cells and Integration with 3D Device Physics

Artit Wangperawong^a, Carl Hägglund^b, and Stacey F. Bent^{b*}

^aDepartment of Electrical Engineering, Stanford University, Stanford, CA, United States

^bDepartment of Chemical Engineering, Stanford University, Stanford, CA, United States

ABSTRACT

We study the optical response of various nanojunction solar cell architectures and examine how various cylindrical arrangements of emitter, base, glass and transparent conductor affect reflection and absorption of incident light. The photogeneration profiles of such nano-architectures are cylindrically asymmetric, varying axially, radially and azimuthally within the wavelength band investigated. Such 3D profiles require 3D device models for accurate device analysis. The extended nanojunction configuration was examined in more detail, as this design is known to have superior performance. The particular design consists of nanostructured glass and a superstrate arrangement of the other device elements.

Keywords: solar cell, photovoltaics, nanostructure, modeling, simulation, 3D, three dimensional, CdTe

1. INTRODUCTION

We previously modeled the three-dimensional (3D) device physics of high aspect ratio nanojunction solar cell architectures (see Fig. 1). Using material properties of CdTe and CdS as a test case for the general model, we demonstrated the conditions under which nanojunction geometries outperform planar junction devices.¹ When using low-quality absorbers, i.e. high doping, low minority carrier mobility and low minority carrier lifetime in the CdTe, the nanojunction architectures were shown to maintain significantly higher short-circuit current than the equivalent planar device. This advantage resulted in higher power conversion efficiencies for the nanojunction designs than for the planar device, despite the lower open-circuit voltages accompanying the nanojunction geometries.

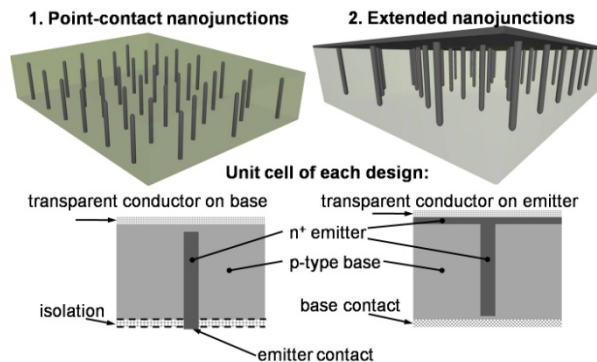


Figure 1. Two nanojunction architectures used in previous device modeling along with the corresponding unit cell for device physics simulations. Sunlight shines on the devices from the top.

*sbent@stanford.edu; phone 1 650 723-0410; fax 1 650 723-9780; bentgroup.stanford.edu

With reference to Fig. 1, the different nanojunction architectures differ mainly by the geometry of the pn junctions and how contact is made to each side of the junction. While the point-contact geometry involves free standing nano-pillars, the extended device can be viewed as a superposition of a planar junction with nano-pillars extending downwards.^{2,3} Emitter contact to the extended device can be made on the entire top side, e.g., via a transparent conductor. For the point-contact device, there is isolation between the bottom emitter contact and the base. The vertical nano-pillars penetrate through the layer of isolation and emitter contact can be made locally at the base of each pillar. In both geometries described above, the base and emitter structures comprise a matrix of interdigitated nanojunctions arranged in a hexagonal lattice (Fig. 2).

The device physics of the two nanojunction geometries were modeled by solving the 3D diffusion-collection equation

$$\frac{1}{r} \frac{\partial}{\partial r} \left(r \frac{\partial \varphi_m}{\partial r} \right) + \frac{\partial^2 \varphi_m}{\partial z^2} - \frac{1}{L_m^2} \varphi_m = 0 \quad m = 1, 2, \quad (1)$$

and applying the reciprocity theorem.^{1,4} The latter states that both dark minority carrier concentration and photogenerated carrier collection obey the same diffusion equation.⁵ It applies to arbitrary 3D geometries with arbitrary doping profiles and variable bandgap, including abrupt compositional changes, grain boundaries and floating junctions.⁶ Our current-voltage calculations were thus greatly simplified by exploiting the reciprocal relationship between dark carrier distribution and photogenerated carrier collection.

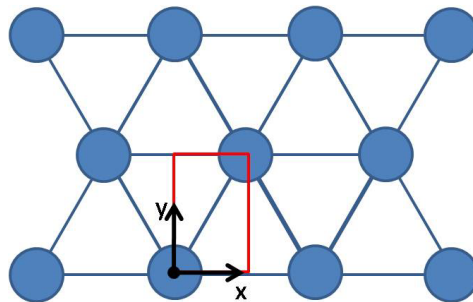


Figure 2. The hexagonal lattice assumed for the arrangement of the nanopyllars. The rectangular unit cell used in our optical simulations is shown in red. Reflective boundary conditions were imposed along the unit cell boundaries.

In order to compare how different nanojunction geometries affect solar cell performance solely from the electronic device perspective, we assumed in previous studies a perfect transparent conductor for all the architectures. With this assumption, there was no reflection and most of the optical losses were due to parasitic absorption in the heavily doped emitter, which was CdS, since the absorption of high-energy photons in the CdS does not contribute significantly to photocurrent. In the current study we first present the results of optical simulations of bare nanojunctions in air to illustrate this point.

To model the overall optical response of a given device as one would manufacture it in practice, however, specifications on the arrangement of other device elements—e.g. the glass and the transparent conductor—around the nanojunctions are necessary. We therefore also investigate here the optical response of one realistic arrangement of the device elements using 3D FEM simulations in Comsol Multiphysics. Specifically, we identify the main sources of optical losses and explain how to use the 3D optical simulation results as input to the 3D device model previously developed.

1.1 RESPONSE OF BARE NANOJUNCTIONS IN AIR

First we present the modeled optical response of the two nanojunction architectures of Fig. 1 in air without any transparent conductors incorporated. The pillar radius, the unit cell radius and the absorber thickness are 25 nm, 110 nm and 1 μm, respectively. The thickness of the top n⁺ emitter layer is 50 nm for the extended device. All surfaces are assumed to be free of roughness. The unit cell for the hexagonal lattice used in the optical simulations is shown in Fig. 2. Note that it uses reflective boundary conditions as previously described⁷ and differs from the unit cell used for device

simulations. The average absorbance was obtained from the two orthogonal polarizations along the x- and y-directions in Fig. 2 at normal incidence of light.

Results shown in Fig. 3 indicate that the primary loss mechanisms are parasitic absorption in the CdS and front-side reflection. The extended geometry contains a larger volume of CdS, especially at the front surface, and as a result exhibits more parasitic absorption for photons with energy above the bandgap of CdS. Although the point-contact design is advantageous due to its use of less CdS, in practice this advantage could be outweighed by the increased number of photogenerated electron-hole pairs lost to surface recombination at the front contact.

For photons with energy below the bandgap of CdS, the extended geometry maintains higher absorption for all wavelengths. This is due to the anti-reflective properties of the planar CdS on the front surface. Overall, the extended design is optically superior because it has higher AM 1.5G spectrally-weighted absorption in the CdTe. Barring new physical effects such as photonic crystal formation, note that the optical characteristics discussed here would also be observed if other pillar sizes and spacing were used. For the particular dimensions chosen here, spectrally-weighted absorbance in the CdTe layer is 69% and 72% for the point-contact and extended geometries, respectively.

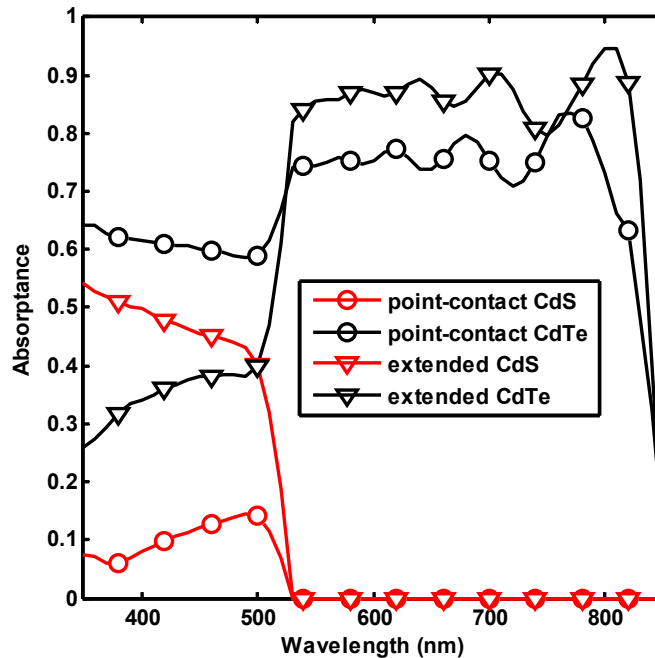


Figure 3. Optical response of the emitters and absorbers of the point-contact and extended nanojunction geometries.

Although in practice for a complete device the reflective losses mentioned above may be reduced by inserting a transparent conductor with refractive indices between that of CdS and glass (CdTe and glass for the point-contact case), a real transparent conductor may also serve as a source of parasitic absorption. Furthermore, if for the point-contact geometry both the emitter and base contacts are placed in the back, the reflection losses will be maintained because there is no thin film on the front-side to reduce reflection. In the following section we explore the optical properties of a complete planar device and one practical embodiment of the extended device architecture, including the glass and transparent conductor.

1.2 RESPONSE WITH GLASS AND ITO

We first consider a planar CdS/CdTe device stack on soda-lime glass (SLG) with 250 nm indium tin oxide (ITO) transparent conductor, 50 nm CdS and 500 nm CdTe, as shown in Fig. 4. A perfect reflector is assumed on the back of the cell. Fig. 5 shows the optical response of the various device layers of this planar cell. Short wavelength photons are lost due to parasitic photogeneration in the CdS as discussed above.

With the addition of ITO to the planar cell, the front-side reflection can be reduced, but additional absorption losses are incurred especially for wavelengths on the upper and lower edges of the spectrum of interest. While the short

wavelength photons are lost due to interband transitions, i.e. photogeneration of electron-hole pairs as in the CdS, the long wavelength photons are lost due to free-carrier absorption in the ITO. Both processes are parasitic and do not contribute to photocurrent. The extended nanojunction architecture to be discussed below exhibits opposite trends—front-side reflection increases, whereas losses in the CdS and ITO are reduced.

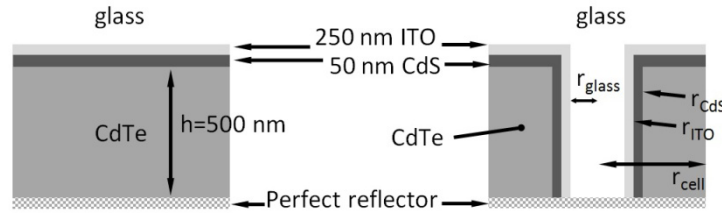


Figure 4. Planar and extended designs used for optical simulations. With respect to the center axis of the pillar, r_{glass} , r_{ITO} , r_{CdS} , r_{cell} are 55 nm, 65 nm, 75 nm and 150 nm, respectively.

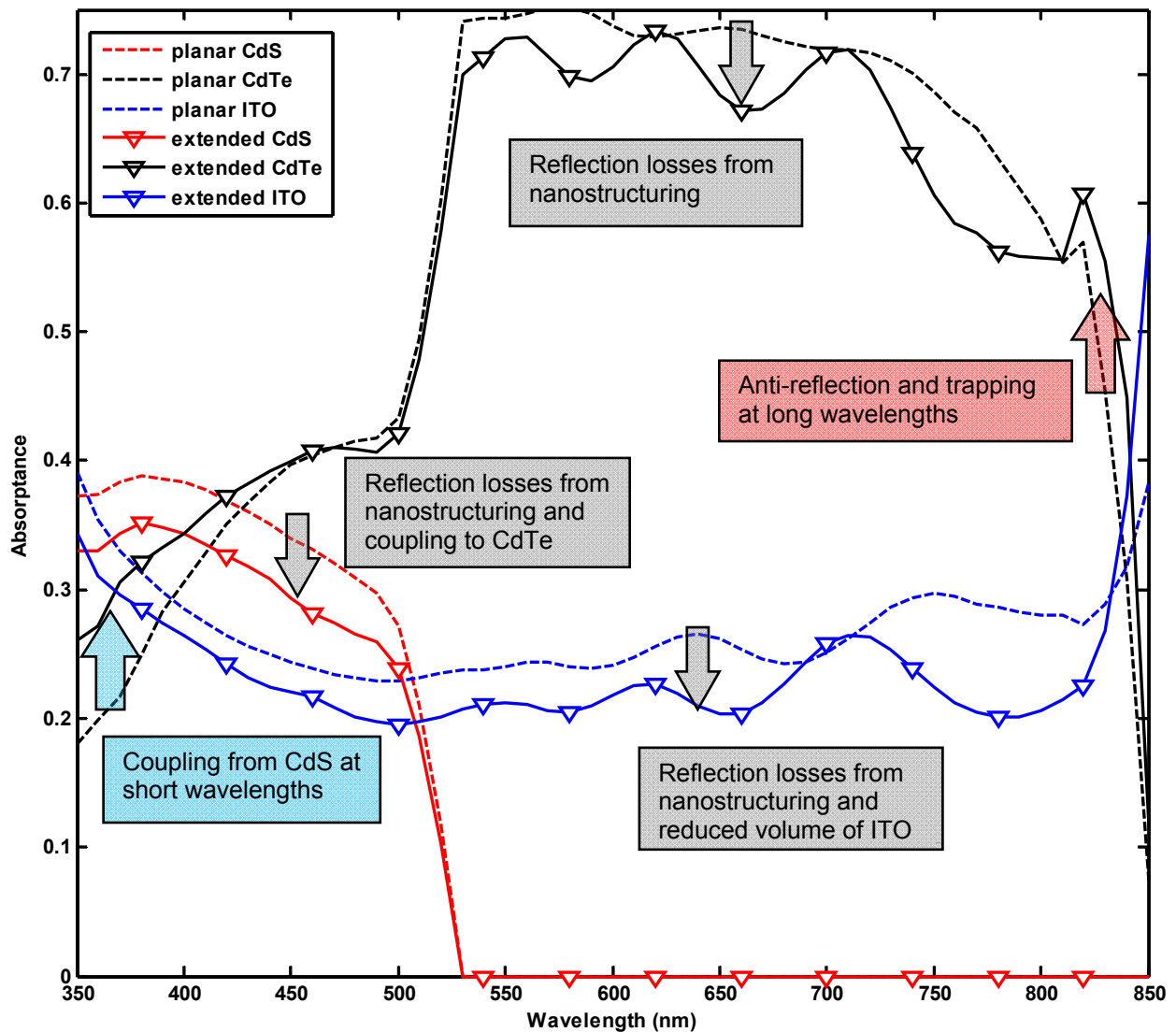


Figure 5. Optical response of planar and extended nanojunction solar cell devices using a SLG/ITO/CdS/CdTe stack and assuming a perfect backside reflector.

We chose the extended nanojunction geometry to add SLG and ITO to because it was shown to outperform the other nanojunction designs previously considered.¹ We also wanted to study a design that could feasibly be realized given existing technology. It has been demonstrated that 80 to 400 nm diameter pillars can be produced with reactive ion etching of quartz.⁸ Assuming similar nanostructures are possible with SLG, here we use 110 nm pillars and add the remaining device layers as would be done in the superstrate fashion, a typical process for CdTe devices⁹ (see Fig. 4). Note that although optically the extended nanojunction of Fig. 4 differs from the extended nanojunction of Fig. 1, they are electronically the same. In other words, holes and electrons in the CdTe do not perceive the glass pillar within the CdS layer.

Since the nanopillar structure has dimensions smaller than the wavelengths of interest, the average refractive index throughout the device is lowered for incoming light. One might therefore expect lower reflection losses in the extended design than for the planar device. This is, however, not the case here. Simulations show that the AM 1.5G spectrally-weighted reflectance is 5.9% and 11.4% for the planar and extended devices of Fig. 4, respectively. This disparity is most likely due to the use of a perfect back reflector in combination with a thin CdTe absorber layer. Thus a thicker CdTe layer may reduce reflection losses.

The extended nanostructure device also exhibits reduced parasitic absorption in both the CdS and ITO layers (Fig. 5). This may be surprising given the increased volume of CdS due to the nanostructuring. However, since the extra volume is wrapped around the vertical nano-pillar, it appears to couple light to and boost absorption in the CdTe, especially at short wavelengths. This is best illustrated in Fig. 6 at 450 nm wavelength of incident light. We are still studying the exact mechanism giving rise to this coupling effect.

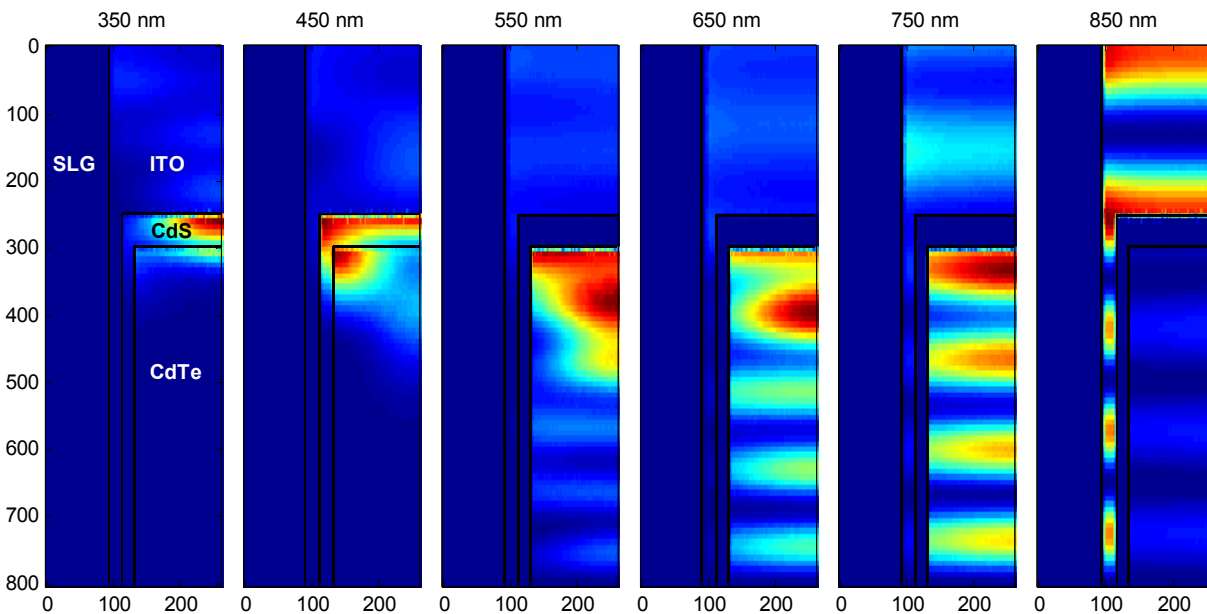


Figure 6. Average absorption profiles at various wavelengths of interest for a vertical slice of the extended design shown in Fig. 4. Maximum to minimum absorption is colored red to blue. Scale on horizontal and vertical axes is in nanometers.

Note that the volume of ITO has decreased in comparison to the planar cell given the dimensions used here. This is most likely the reason for reduced absorption in the ITO for much of the spectrum. At long wavelengths beyond 825 nm, however, a light trapping effect boosts absorption in both CdTe and ITO. Given all the effects described thus far, the overall spectrally-weighted absorptance in the CdTe layer is 59.9% and 58.3% for the planar and extended devices, respectively.

In order to further reduce parasitic absorption in the ITO and CdS, one may find it desirable to construct a complete device using the extended nanojunction geometry with as little volume of ITO and CdS as possible. One possible arrangement is to keep the glass and ITO planar, nanostructuring only the CdS. The device could then be optically superior while maintaining the same device physics advantages provided by the extended nanojunction geometry.

Although we have yet to model this architecture, such a design may on the other hand show less light trapping and coupling as described above and also less light confinement which is potentially beneficial as described below.

Figs. 6 and 7 show that for all wavelengths within the extreme edges of the spectrum of interest (500 to 800 nm) CdTe absorption is mostly confined in the CdTe away from the metallurgical interface. This confinement effect is accentuated deeper into the CdTe, as shown in Fig. 6. Interestingly in Fig. 6 at 450 nm wavelength, the absorption near the top is actually more localized to the horizontal and vertical metallurgical junctions than other wavelengths. This is due to a different light coupling effect described previously above.

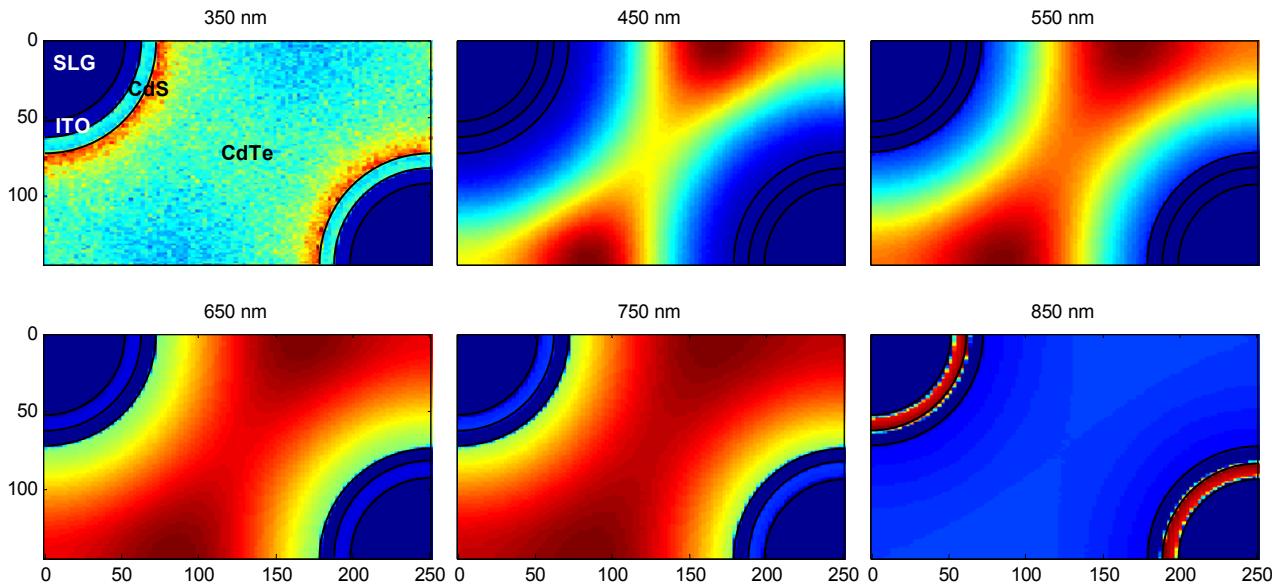


Figure 7. Average absorption profiles at various wavelengths of interest for a horizontal, in-plane slice 150 nm into the CdTe of the extended design shown in Fig. 4. Maximum to minimum absorption is colored red to blue. Scale on horizontal and vertical axes is in nanometers.

Confinement away from the metallurgical junction may be electronically beneficial because interface states can serve as recombination centers for photogenerated electron-hole pairs. This effect would be important for nanojunction geometries, especially given the increase in surface area as compared to the planar junction and given that the heterojunction is not lattice-matched in polycrystalline thin films.

If the device is not fully depleted and operates in the long base regime (i.e. dark minority carrier concentration in the CdTe absorber reaches its equilibrium value because inter-pillar spacing is wide enough), such confinement away from the collection surface of the depletion edge means that the collection probability is lower. Thus there is a tradeoff between collection probability and interfacial recombination as explained above. If the device is near full depletion, then photogeneration away from the metallurgical junction can offer net benefits.

1.3 INTEGRATION WITH DEVICE PHYSICS

Most existing theoretical studies on nano-geometries have cylindrically integrated two-dimensional numerical optics simulations, imposing unit cell boundary conditions which do not account for the electronic connection between nanojunctions in an interdigitated device.^{10,11} Such an approach also requires azimuthal averaging of the optical absorption data and does not account for 3D variation in the photogeneration profiles demonstrated in the nano-architected devices studied here. Full 3D analysis has not been practical numerically due to the computational resources required.

To address these issues, we recently introduced an analytical approach for studying 3D nano-architectures that can be broadly applied to both isolated and interdigitated geometries of various forms. To the best of our knowledge, this

approach is currently the only reported 3D device physics model on high aspect ratio nanostructures that can accommodate photogeneration profiles with axial, radial and azimuthal variation, which is necessary for our nano-architected solar cells as explained below.

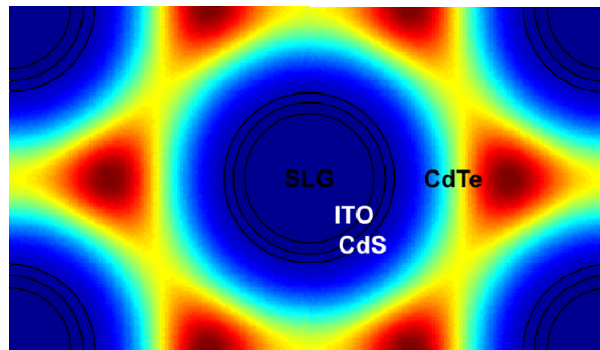


Figure 8. Absorption profile of a horizontal in-plane slice 150 nm into the CdTe of the extended design shown in Fig. 4 at 450 nm incident light. Here four unit cells are stitched together to demonstrate radial and azimuthal variation for a given device unit cell.

For long wavelengths beyond 750 nm, cylindrical integration of flattened 2D profiles may be an appropriate approximation in our case. For the bulk of the spectrum at shorter wavelengths, however, this approximation is less accurate. Fig. 8 illustrates this with the absorption profile of a horizontal in-plane slice located 150 nm into the CdTe at 450 nm wavelength. Four optical unit cells are stitched together to show that much of the absorption is cylindrically asymmetric and confined in the CdTe.

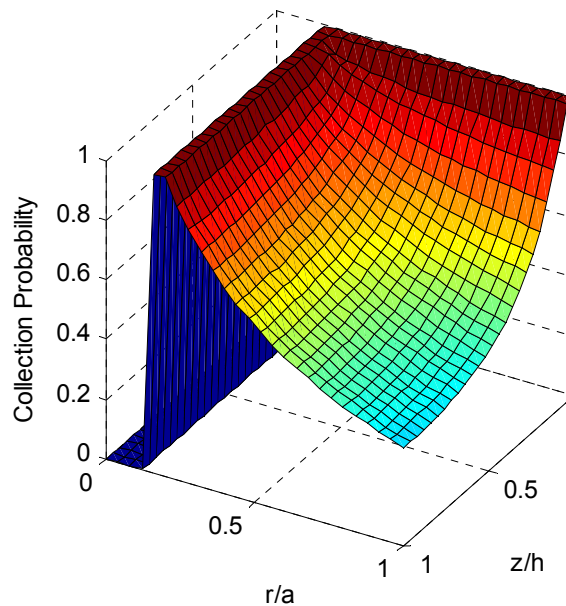


Figure 9. Carrier collection probability profile of an extended nanojunction geometry.

Employing the reciprocity theorem relating dark carrier distribution to photogenerated carrier collection, our model allows us to multiply the photogenerated carrier collection probability by the photogeneration profile and to integrate over the entire volume of the device in three dimensions. Fig. 9 shows an example of the carrier collection probability for the extended nanojunction geometry. It can be seen that the collection probability within and nearby the CdS ($r/a \sim 0$) is nearly zero, illustrating our earlier statement about the photogeneration within the CdS and at the metallurgical

junction. In any case, this collection probability can be multiplied by the 3D data of Figs. 6, 7 and 8 to calculate not only current at a given applied bias but also the internal and external quantum efficiencies, i.e. IQE and EQE. Such work is currently in progress.

CONCLUSION

In this study we characterize the optical response of various nanojunction architectures and explain how placement of device elements such as the glass and transparent conductor affect reflection and absorption. We also show that at various wavelengths of incident light, the photogeneration profiles of the nano-architected devices are not cylindrically symmetric but vary significantly along the radial, axial and azimuthal coordinates, requiring 3D device models to capture for accurate device analysis. The extended nanojunction design was chosen for its robustness and superior performance, and one realistic embodiment of how SLG and ITO can be incorporated into the design is presented. An approach was outlined for future work incorporating the optical simulation results into the 3D device model to generate current, voltage and power data for the various nano-architected devices, including the glass and transparent conductor.

ACKNOWLEDGEMENTS

Studies were carried out as part of the Center on Nanostructuring for Efficient Energy Conversion, an EFRC funded by the U.S. Department of Energy, Office of Basic Energy Sciences under Award No. DE-SC0001060. A.W. acknowledges financial support from the DOE, Office of Science Graduate Fellowship Program, made possible in part by the American Recovery and Reinvestment Act of 2009, administered by ORISE-ORAU under Contract No. DE-AC05-06OR23100, and support from National Science Foundation under Grant No. CBET 0930098. C.H. acknowledges the Marcus and Amalia Wallenberg's Foundation for financial support.

REFERENCES

- [1] Wangperawong, A. and Bent, S. F., "Three-dimensional nanojunction device models for photovoltaics," *Appl. Phys. Lett.* 98, 233106 (2011).
- [2] Peng, K.-Q. et al., "High-Performance Silicon Nanohole Solar Cells," *J. Am. Chem. Soc.* 122, 6872-6873 (2010).
- [3] Fan, Z. et al., "Three-dimensional nanopillar-array photovoltaics on low-cost and flexible substrates," *Nature Mater.* 8, 648-653 (2009).
- [4] Wangperawong, A. and Bent, S. F., "Modeling Performance of Three-Dimensional Nanojunction Photovoltaic Devices," 37th IEEE Photovoltaic Specialists Conference, (2011).
- [5] Donolato, C., "A reciprocity theorem for charge collection," *Appl. Phys. Lett.* 46, 270 (1985).
- [6] Green, M. A., "Generalized relationship between dark carrier distribution and photocarrier collection in solar cells," *J. App. Phys.* 81, 268-271 (1997).
- [7] Hägglund, C., Zäch, M., Petersson, G. and Kasemo, B., "Electromagnetic Coupling of Light into a Silicon Solar Cell by Nanodisk Plasmons," *Appl. Phys. Lett.* 92, 053110 (2008).
- [8] Xie, C., Hanson, L., Cui, Y. and Cui, B., "Vertical nanopillars for highly localized fluorescence imaging," *PNAS* 108, 3894-3899 (2011).
- [9] Luque, A. and Hegedus, S., [Handbook of photovoltaic science and engineering], Wiley, West Sussex, (2003).
- [10] Kapadia, R., Fan, Z. and Javey, A., "Design constraints and guidelines for CdS/CdTe nanopillar based photovoltaics," *Appl. Phys. Lett.* 96, 103116 (2010).
- [11] Kelzenberg, M. D., et al., "Predicted Efficiency of Si Wire Array Solar Cells," 34th IEEE PVSC, 1948-1953 (2009).